Tuning particle settling in fluids with magnetic fields

Facundo Cabrera-Booman,[1,2] Nicolas Plihon,[2] Raúl Bayoán Cal,[1] and Mickaël Bourgoin[2]
[1)] *Department of Mechanical and Materials Engineering, Portland State University, Portland, Oregon, USA.*
[2)] *Univ Lyon, ENS de Lyon, CNRS, Laboratoire de Physique, F-69342 Lyon, France.*

(Dated: 22 August 2025)

A magnetic field is generated to modify the effective gravity acting on settling particles in a laboratory experiment. When applied to a magnetized spherical particle settling in water-glycerol mixtures, the magnetic field produces a vertical force that counteracts the gravitational field, hence allowing for the magnetic tuning of the settling properties of the particle. While doing so, the spin of the particle around the direction perpendicular to the applied magnetic field is blocked, thus allowing spin solely around the direction of the magnetic field. This method of magnetic modification of the effective gravity is tested on the settling of spherical magnets in quiescent fluids over Galileo numbers in the range $[100, 300]$, and a fixed particle density of 8200 kg/m^3. The results obtained by varying the Galileo number via the magnetic modification of effective gravity are compared to those obtained with non-magnetic spheres when the Galileo number is modified by varying the fluid's viscosity. We show that the same taxonomy of settling regimes, with nearly identical geometrical properties (in terms of planarity and obliqueness) of the trajectories are recovered. In addition to proving that it is possible to magnetically tame the settling of particles in fluids preserving the features of the non-magnetic case, this also reveals that blocking the spin of the particles does not produce any significant effect on its settling properties in a quiescent fluid. This novel experimental methodology opens new possibilities to experimentally explore many other subtle aspects of the coupling between settling particles and fluids (for instance, to disentangle the effects of rotation, inertia, and/or anisotropy of the particles) in more complex situations including the case of turbulent flows.

I. INTRODUCTION

It is of the utmost difficulty to reduce or suppress the effect of gravity in a laboratory on Earth. In the context of particle-laden flows research, only a handful of very particular situations allow for the suppression of gravity, such as the use of neutrally buoyant particles. This prevents the exploration of crucial particle-fluid mechanisms including inertial effects, which are related to particle-to-fluid density ratio. The means available to do experimental research in a low gravity environment while preserving the capacity to explore inertial effects due to density differences are expensive, scarce, and lack repeatability. The only options are drop towers, parabolic flights, or space experiments in the International Space Station[1–3]. In this article, we present a method to compensate the gravity acting on a particle in a flow by the application of a magnetic induction (the terms "magnetic field" and "magnetic induction" will be used interchangeably in this article). With this purpose and as a proof of concept, we revisit the problem of the settling of spherical particles in a quiescent fluid[4–9] while the effective vertical force experienced by the particles is magnetically varied. Relevant research is present in the literature and a brief summary follows.

Research on the use of magnetic fields for gravity compensation purposes has been mostly conducted on diamagnetic objects, e.g., DNA, water, or proteins. For instance, when ways to circumvent Earnshaw's theorem came to light[10,11], it was possible to levitate living diamagnetic objects such as frogs[12]. These studies led to the technique of high-gradient magnetic separation that allows the sorting of sample components with different magnetic susceptibilities[13–15]. In parallel, the Magnetic Resonance Imaging community developed the technical aspects to achieve an arbitrary magnetic field profile in a laboratory (or a hospital) with the use of coils[16,17]. These are apart from the study of particles in conductive fluids under the influence of external magnetic inductions, which are central to a number of industrial situations, such as clean metal production[18]. The profiles of the external magnetic induction needed to obtain a constant vertical force that can counteract gravity in a number of scenarios such as liquid helium or oxygen were also studied[19–22]. With these tools in hand, some progress has also been made in the particular situations that interest this article: paramagnetic/ferromagnetic or permanently magnetized particles in a weak diamagnetic liquid (i.e., water) subjected to a *weak* external magnetic induction environment (thus no liquid magnetisation occurs). Some studies explored the effects of a homogeneous magnetic induction on one or more particles in non-magnetic fluids[23–27]. In these studies, the main focus was exploring the role of particle-particle interactions on their coupling with the fluid, using a homogeneous magnetic field as a way to tune interactions between particles.

In this article, we focus on the control of the settling of single magnetized spherical particles in a quiescent flow, using an externally applied magnetic field to modify the vertical force acting on the particles. The rich dynamics of single spheres settling in quiescent flows has been extensively explored using numerical[6,7,28,29] and experimental tools[4,5,8,30]. The settling of spheres in a quiescent viscous fluid is controlled by two non-dimensional parameters: (i) the particle-to-fluid density ratio Γ, and (ii) the Galileo number $\mathrm{Ga} = U_g d_p/\nu = \sqrt{|\Gamma-1|g d_p} d_p/\nu$, with U_g the buoyancy velocity, d_p the particle diameter, g the local acceleration of gravity, and ν the kinematic viscosity. The diversity of settling regimes has been represented in the $\Gamma-\mathrm{Ga}$ parameter space[7,8,30]. As Ga increases, the trajectory dynamics exhibit bifurcations between different regimes such as rectilinear, steady oblique, oscillating oblique, rotating, or chaotic (see fig. 5). Note that, for a given density ratio Γ, the Galileo number may be changed either by changing the particle's diameter or the fluid viscosity. This problem thus offers an appealing framework to validate a magnetic method to tune the effective vertical force experienced by a particle. In this article, we explore how the $\Gamma-\mathrm{Ga}$ parameter space is modified when an additional constant magnetic force is applied to the particles. Bifurcations between regimes and properties of the trajectory collapse when using a corrected Galileo number $\mathrm{Ga}(\tilde{g})$ that considers the effective gravity $\tilde{g}$ in its computation. In order to explore $\mathrm{Ga}(\tilde{g})$ ranging from 100 to 280, we varied not only the magnetic vertical force but also the viscosity of the fluid.

The article is organized as follows. We first present the basic theoretical layout of the magnetic gravity compensation method and experimental design in Section II. The results of the sedimentation of magnetic particles with modified gravity are described in Section III. Then, we discuss conclusions and perspectives of this work in Section IV. Finally, the Appendix presents further details on the theoretical foundation of the method, its validation, and further experimental details.

II. GRAVITY TUNING USING MAGNETIC FORCES

A. General Principles

The method introduced in this article consists on the application of a constant vertical magnetic force to a magnetized particle in order to modify the effective vertical force it experiences. The forces applied are the magnetic force $\mathbf{F}^M$, the weight, and the fluid force $\mathbf{F}^{\text{fluid}}$ exerted by the fluid to the particle. Similarly, a magnetic torque $\mathbf{T}^M$ adds up to the fluid torque $\mathbf{T}^{\text{fluid}}$. In this section, we discuss the features of the externally applied magnetic field required to modify the vertical force on small spherical permanent magnets.

The magnetic torque and force acting on a particle with a magnetic dipole $\mathbf{M}$ in the presence of an external magnetic induction $\mathbf{B}$ read:

$$\mathbf{F}^M = \nabla(\mathbf{M}\cdot\mathbf{B}), \tag{1}$$

$$\mathbf{T}^M = -\mathbf{M}\times\mathbf{B}. \tag{2}$$

These equations indicate that the magnetic force and torque can be varied independently by the gradient and magnitude of B, respectively. We focus on the modification of the vertical force along the $\hat{z}$ axis, which reads:

$$\mathbf{F}\cdot\hat{\mathbf{z}} = m\tilde{g} = m\big[g + \mathrm{M}\nabla_z(B)\cos(\psi)/m\big], \tag{3}$$

where the effective gravity $\tilde{g}$ was defined, $B = |\mathbf{B}|$, and ψ is the angle between the vectors $\mathbf{B}$ and $\mathbf{M}$. See the full equation of motion in App. A 1. The method aims at reaching a constant value of $\tilde{g}$ over the settling of the small permanent dipole and requires: (1) a constant ψ angle and (2) a linear evolution of the vertical component of the magnetic field $B_z = G_z\ z + B_0$, where the gradient G_z sets the amplitude of the vertical magnetic force and B_0 is an offset value. Condition (1) is met when the magnetic torque exceeds the hydrodynamic torque, a condition which is always met in our configuration, as discussed below. A limitation of the method comes from the existence of a radial force, due to the radial component of the magnetic field in cylindrical coordinates, imposed by the divergence-free nature of magnetic fields. Indeed, condition (2) imposes the following magnetic field evolution (see App. A 2):

$$\mathbf{B}(r,z) = (G_z\ z + B_0)\ \hat{\mathbf{z}} + (-G_z/2\ r)\ \hat{\mathbf{r}}. \tag{4}$$

The relative intensity of the undesired radial drift is controlled by both the value of the axial gradient G_z and the offset B_0 (see App. A 2 for a full derivation of the force). In order to minimize spurious effects of magnetic radial drift, we have designed our experiment choosing values of G_z and B_0 (see Table III) so that the ratio between the radial and axial magnetic forces within the measurement volume (see Eq. E7) remains smaller than $5\cdot 10^{-2}$.

Conversely, the magnitude of the torque can be quantitatively estimated. Given the expression of the linear magnetic field given by Eq. (4), the ratio of the magnetic torque over the hydrodynamic torque reads (see App. A 2 for complete derivation):

$$T^M/T^{\text{fluid}} = \frac{|\mathbf{M}||\mathbf{B}|}{1/64 C_\omega d_p^5 \pi \rho_f \omega^2}, \tag{5}$$

where d_p is the particle diameter, $|\mathbf{M}|$ its magnetic moment, ω the particle angular velocity, C_ω the rotational drag coefficient, and ρ_f the fluid density. The value of the torque ratio is of the order of 10^{11}, based on the typical values used in our experiment[31]. This implies that the magnetic dipole aligns with the magnetic field virtually instantaneously and the particle rotation is therefore only possible around the direction of the magnetic field.

B. Experimental Setup

The experiments are performed in a transparent PMMA water tank with a square cross-section of 170 ×

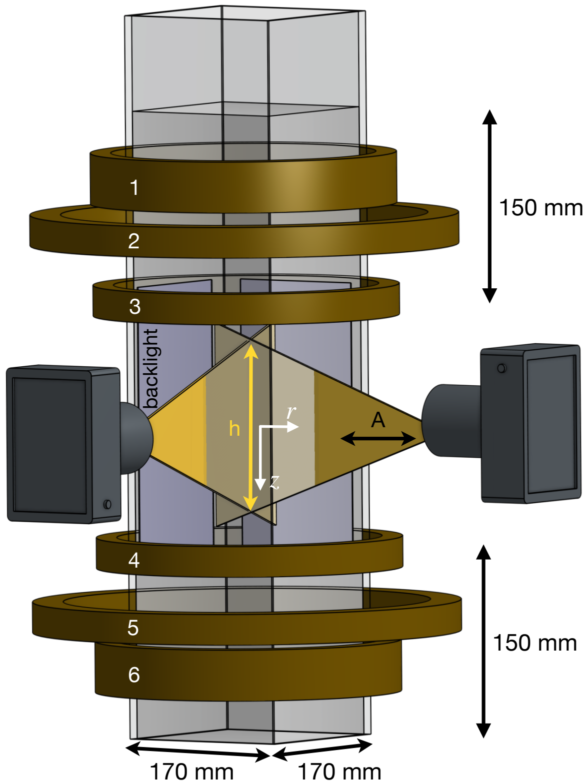

FIG. 1. Experimental setup. Two cameras image the particles inside the water tank. Six circular coils produce a magnetic induction used to compensate gravity on magnetic particles. The origin of coordinates is located at the geometrical center of the water tank, which coincides with the middle distance between coils 1 and 6.

170 mm^2 and a height of 710 mm, which is sketched in Fig. 1. The tank is filled with different mixtures of pure glycerol (Sigma-Aldrich W252506-25KG-K) and distilled water, ranging from 0% to 40% glycerol concentration. Viscosity is measured with a rheometer Kinexus ultra+ from Malvern industries with a maximum uncertainty of 0.6%. The kinematic viscosity ν ranges from 1×10^{-6} to 1×10^{-3} m^2/s. Furthermore, an air-conditioning system keeps a constant room temperature of (22 ± 0.6)°C yielding a 2% uncertainty on the precise value of the viscosity.

A 150 mm region of fluid above and below the visualization volume is set to ensure both the disappearance of any initial condition imposed on the particles when released and the effects of the tank's base. Furthermore, a minimum distance of 20 mm between the tank walls and the particles is maintained. Using available correlations[32], the settling velocity hindering due to wall effects is estimated to be lower than 3%, thus neglected.

To record the trajectory of the particles, two high-speed cameras model fps1000, from The Slow Motion Company, image the water tank with a resolution of 720×1280 px^2 and 2300 Hz. Backlight illumination is used, as represented by the dark blue rectangles in Fig. 1. These dual recordings allow the implementation of a 4D-LPT (Lagrangian Particle Tracking resolved in time and in three dimensions)[33]. This method accurately tracks particles with a precision of approximately 90μm. This level of precision is determined by assessing the disparity between rays during the stereo-matching process between the two cameras. It is important to note that the experimental noise affecting particle position is short-term in nature. This noise is effectively mitigated due to the temporal redundancy achieved through oversampling at a high frame rate of 2300 Hz. In order to reduce experimental noise (due to inevitable particle detection errors in the Lagrangian particle tracking treatment[34]), the raw trajectories are smoothed by convolution with a Gaussian kernel of width $\Sigma = 12$ frames; acting as a low-pass filter with a cut-off frequency $f_c = 2300$ Hz$/\Sigma = 192$ Hz. Consequently, the uncertainty associated with instantaneous velocity along these trajectories is less than 4 mm/s[33]. Moreover, when the velocity is averaged over a specific trajectory, the associated uncertainty of the mean velocity decreases to a few hundred microns per second.

The particles are spherical permanent neodymium magnets with a mass density $\rho_p = 8200$ kg/m^3, a diameter $d_p = 1$ mm, and an average arithmetic roughness

$$Ra = \frac{1}{L_x L_y}\int_0^{L_x}\int_0^{L_y} |z(x,y) - \overline{z(x,y)}|dxdy = 15\ \mu\text{m},$$

where (x, y) is the local planar surface and L_x and L_y are the distances over which the height $z(x, y)$ and its average over the measurement area $\overline{z(x,y)}$ are obtained. These measurements are performed with a Scanning Electron Microscope (SEM) model ZEISS SUPRA 55 VP, over an area of 200×500 µm^2. The surface roughness of particles has been proven to influence the boundary layer, therefore modifying several aspects of the dynamics[35–37]. Note that the small values $Ra/d_p < 1.5 \times 10^{-2}$ are not expected to notably modify the dynamics[36]. Particle dimensions and shapes were measured using a microscope with a precision of 10 μm. No significant deviation from the spherical shape or the documented diameter were measured. The weight of one hundred particles was measured with a precision of 1×10^{-3} g. The result was divided by one hundred to obtain the average mass of a single particle: $m_p = 4.3 \times 10^{-3}$ g with a precision of 1×10^{-4} g.

The ranges of non-dimensional numbers reached are Ga = [100, 280] and Γ = [6.8, 8.2]. Note that the water density is different at each viscosity and therefore Γ varies as well. The magnetic moment $|\mathbf{M}|$ is computed using Eq. E8 and results in $|\mathbf{M}| = 4.96 \times 10^{-4}$ Am^2. The external magnetic induction is created from a six-coil system shown in Fig. 1 and detailed below. While a larger number of coils would produce a magnetic field closer to the linear profile needed, the choice of six coils resulted in the compromise between quality of magnetic field (measured in Sec. II C) and the need for optical access. The coils were wound from copper wires of 0.5 mm (coils 2 to 5) and 1.5 mm (coils 1 and 6) in diameter. The coils are placed at vertical distances Z_i ($i \in [1, 6]$) from the origin of coordinates, set at the middle distance between coils

TABLE I. Characteristics of the coils used for the magnetic compensation of gravity. Columns show the following parameters for each coil used: effective number of turns N, radius R, and cross section σ. Each coil is represented by a number as in Fig. 1.

	1	2	3	4	5	6
N	965	103	450	452	101	969
R (cm)	16.3	22.1	15.6	15.4	21.8	16.1
σ (cm^2)	15.6	3.9	3.6	3.6	3.9	15.6

1 and 6. Details on the position of coils and the current imposed are available in App. B.

C. Magnetic Field Generation

The system of coils generating the magnetic induction is described in detail in what follows. Each coil has a radius R_i and a current I_i. In order to simplify computations, each coil is modeled as a single loop of radius R_i with an effective current $N_i I_i$ (N_i is the effective number of turns). The value of N_i is determined from a nonlinear fit of experimental measurements of the magnetic induction using a Bell 7030 Teslameter by:

$$B_i(z) = 2\pi 10^{-7} \frac{R_i^2 N_i I_i}{(z^2 + R_i^2)^{3/2}}, \qquad (6)$$

where z is the distance from the coil i's individual geometric center.
The coils' effective parameters are presented in Table I. The uncertainties on N_i and R_i by the aforementioned method are estimated to be 4% and 3%, respectively, while the coils' cross-section (σ) uncertainty is 0.4 cm^2. Note that three sets of identical coils were used (namely 1-6, 2-5, and 3-4), and the uncertainties of their effective parameters are identical.

The six circular coaxial coils used to generate the required magnetic induction (Eq. 4) are sketched in Fig. 1. The coils are modelled as infinitesimal current loops, therefore the theoretical axial magnetic induction at the six-coil system axis reads:

$$\mathbf{B} \cdot \hat{\mathbf{z}} = 2\pi 10^{-7} \sum_{i=1}^{6} \frac{R_i^2 \ N_i \ I_i}{((z + Z_i)^2 + R_i^2)^{1.5}}. \qquad (7)$$

In order to set the magnetic field presented in Eq. 4 in the laboratory, a nonlinear least squares fit of Eq. 7 to the axial component of Eq. 4: $B_z = \mathrm{G_z}\ \mathrm{z} + \mathrm{B_0}$ is performed. The fit's fixed parameters are: N_i, R_i, G_z, B_0, and Z_{fit} the range at which the fit is performed . The outputs are: I_i the current in each coil, and Z_i the distance between the coil i's geometrical center and the origin of coordinates $z = 0$ (located at the middle distance between coils 1 and 6). This method to solve equations numerically is not affected by the fact that there are more variables than equations, as the variables are modified at random until the coefficient of determination (R^2) is minimized.

TABLE II. Details of the two external magnetic inductions implemented here: Case g_0 and $g^* = 0.65$.

	Nonlinear fits		Measurements	
	Case g_0	Case $g^* = 0.65$	Case g_0	Case $g^* = 0.65$
G_z (G/m)	0	-290	0 ± 20	-286±25
B_0 (G)	20	26	20±1	22±1
Z_{fit} (mm)	(-150, 50)	(-100, 0)	✗	✗

Note that there is no radial dependence on Eq. 7. The magnetic field outside the axis is estimated by Maxwells' equations in App. A 2 (see Fig. A.1). This theoretical prediction was qualitatively confirmed with a Teslameter.

Two sets of values for G_z, B_0, and Z_{fit} were chosen:

1. **Case g_0: homogeneous vertical magnetic induction.**
   In this case $\mathrm{G}_z = 0$ & $B \neq 0$, yielding no net magnetic force and only impacting the particle's rotation through the blocking effect of the magnetic torque previously discussed.

2. **Cases g^*: constant gradient vertical magnetic induction.**
   In this case $G_z \neq 0$ & $B \neq 0$, yielding both a net magnetic force (used to compensate gravity) and a net magnetic torque, resulting in the rotation-blocking effect, respectively.

The two cases differ on the magnetic force magnitude (proportional to G_z) that they impose on the particles: whereas Cases g^* block the rotation and apply a force, Case g_0 blocks the rotation but the applied force is negligible. The size of the fit window Z_{fit} needed to be shortened for Cases g^* to minimize inhomogeneities in the magnetic force. The specific values of these two sets of input parameters in the nonlinear fit to Eq. 7 are presented in Table II, alongside the corresponding magnetic induction measurements discussed below. Details about coils' parameters for both cases are detailed in App. B.

Note that new cases are achieved by the multiplication of the base currents in each coil given by the solutions of Cases g_0 and $g^* = 0.65$.

Fig. 2 presents the profiles of axial magnetic induction B_z (first row) and its gradient $\nabla_z B$ (second row) obtained from the nonlinear fit (black lines), and measurements performed with a Teslameter (blue crosses), versus distance to the origin. Finally, the blue shade represents the region (Z_{fit}) where the fit was performed. Note that because the magnetic field is measured at the axis, the equation fitted represents the center of a current loop $\mathbf{B} = B_z \hat{\mathbf{z}}$.

It can be seen that, for Case g_0, the magnetic induction measurements (Fig. 2(a)) overlap with the simulations, whereas the magnetic induction gradient (Fig. 2(c)) presents an average difference of 10%, with maximum

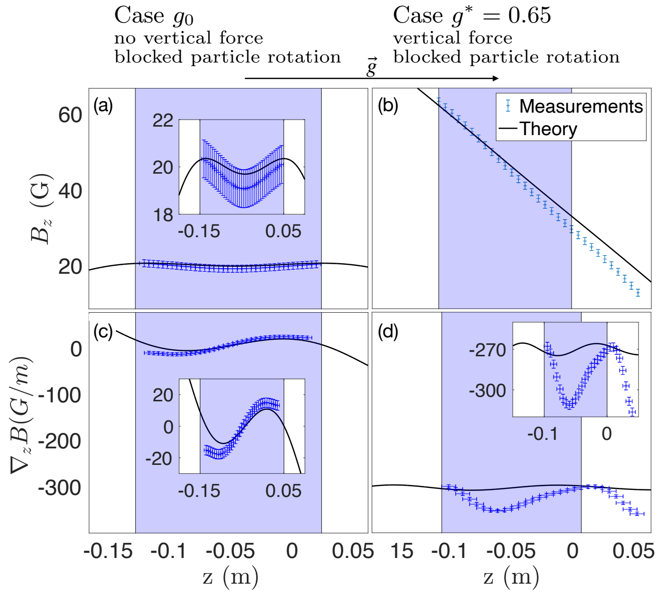

FIG. 2. B_z and its gradient computed from the axial magnetic induction measurements (blue points) and simulations (black line) against the distance to the origin $z = 0$, for Cases g_0 and $g^* = 0.65$. The insets present a zoomed version of the plots. The blue area shows the z-range Z_{fit} over which the magnetic field is optimized. Finally, a horizontal arrow denotes the rightwards direction of gravity.

values of 30% that occur near the extremes of Z_{fit}. On the other hand, Cases g^* have a 10% discrepancy on the magnetic induction gradient $\nabla_z B$ (Fig. 2(d)) and in the magnetic field (Fig. 2(b)). Additionally, note that the radial-to-axial force ratio (Eq. E7) takes the following maximum value for Cases g_0 and g^*: 1×10^{-2} and 1.5×10^{-1}, respectively. In the case of the 1 mm spherical permanent magnets that are studied here, these inhomogeneities in the magnetic induction gradient produce a 5% and 3% of typical variability in the effective gravity value for Cases g^* and g_0, respectively.

The presence of oscillations in the magnetic field can be explained as the interference between the higher harmonics that compose the total magnetic induction of each coil[19]. The interaction between these higher harmonics can be modified considerably by small errors in the coil positioning. To explore this idea, Fig. 3 shows the theoretical magnetic induction (a) and gradient (b) for Case $g^* = 0.65$, evaluated at different coil 1 positions (Z_1): its original position (black), 5 mm downwards (red), and 5 mm upwards (magenta). While the magnetic inductions are indistinguishable (Fig. 3 (a)), the gradients show clear differences (Fig. 3 (b)): Within the measurement region (blue shade) a difference of up to 3% is present. Note that the coil positioning error is estimated to be 5 mm; this value includes the approximation of the coils by an infinitesimal loop at its geometrical centre and the 2 mm precision in positioning due to the tools used. These factors are hypothesized to produce the difference between the experimental measurements and the simulated values encountered in Fig. 2.

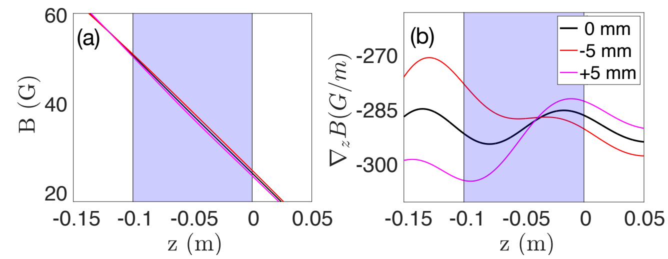

FIG. 3. Theoretical magnetic field (a) and gradient (b) for Case $g^* = 0.65$, evaluated at different coil 1 vertical positions. The original coil position (black); 5 mm downwards (red); and 5 mm upwards (magenta) are shown.

D. Data Sets

The camera-tank distance A was varied to obtain two different measurement volume heights h (see Fig. 1): $h = 100$ mm and $h = 200$ mm which correspond to the ranges Z_{fit}. This translates into different maximum particle non-dimensional trajectory lengths $l^*_{max} = h/d_p = 100$ & 200 (recall that d_p is 1 mm for all cases), while the measured volume has a 150×150 mm^2 transverse section.

The experimental procedure is as follows: Initially, the tank is filled with a water-glycerol mixture and 24 hours are allowed to pass. During this time, the temperature at various locations within the bulk of the fluid stabilizes to a temperature difference of less than 0.6°C. This was determined by a movable temperature probe that was used to measure the temperature in the fluid at different locations. Subsequently, a standard calibration process for the 4D-LPT system is executed[33]. Once calibration is complete, the magnetic field is activated and spherical particles are released from a plastic tube with a 5 mm diameter positioned at the center of the tank and 5 cm above the region of interest. The particles are carefully introduced one by one into the tube where they settle due to gravitational forces. To ensure that the fluid remains undisturbed between successive particle releases, a minimum waiting time of 120 seconds is observed. This interval is chosen to be at least 12 times the viscous relaxation time, denoted as $\tau = d_p^2/\nu$. The specific value of the viscous time varies across experimental cases and a maximum waiting time value of $1 \times 10^3 \tau$ is achieved in the more viscous case.

III. SINGLE MAGNETIC SPHERE SETTLING AT FIXED ORIENTATION AND MODIFIED GRAVITY

In this section the local gravitational pull is reduced via the magnetic gravity compensation method presented previously. It is proven that the Galileo number (and hence the settling regime) of spherical magnetic particles can be magnetically tuned. Furthermore, these results confirm the validity of the magnetic gravity compensation method. This is the first step towards the deployment of a global strategy to experimentally explore the influence of gravity in particle-fluid interactions.

A. Parameters explored

The results of an experimental study on spherical metallic particles settling in a quiescent flow at moderate Reynolds numbers performed by our group[8] are used as reference data to be compared against the present measurements. Note that those experiments were performed in the water tank presented in Fig. 1 and the non-magnetic particles used had $\rho_p = 7950$ kg/m^3, which is comparable to the density of our magnetic particles.

Recall that the particles are affected in two ways due to the presence of the external magnetic inductions produced here: First, as the applied magnetic field is mostly vertical on the region of interest, particle rotation is partially blocked and only allowed around the vertical axis. Second, the spatial profile of the imposed field is specifically tailored to be as close as possible to a homogeneous vertical gradient field in the region of interest, hence particles experience an almost constant magnetic force which counteracts the gravitational force yielding different effective gravity values $\tilde{g}$.

In the sequel, the following nomenclature will be used to refer to the different experiments:

- Case $\emptyset B$
  Reference case with non-magnetic particles[8].
- Case g_0
  Uniform magnetic induction (spin blocking effect). This magnetic induction profile was presented in Fig. 2(a)-(c).
- Cases g^*
  Uniform magnetic induction gradient (spin blocking and modified gravity). The magnetic induction profile was presented in Fig. 2(b)-(d).

As detailed in Section II D, the visualization volume in Case g^* has a maximum non-dimensional height $l^*_{max} = 100$, whereas for Case g_0 $l^*_{max} = 200$. This difference is due to the finite size of the coils: It is possible to produce a homogeneous magnetic induction (Case g_0) in a larger region of space compared to the production of a homogeneous magnetic induction gradient (Cases g^*).

For the Cases g^*, Table III summarizes the different effective gravities $\tilde{g}$ explored (details about the estimation of $\tilde{g}$ are given in the next subsection). The effective gravity will be given from now on in non-dimensional form $g^* = \tilde{g}/g$. In practice, changing the effective gravity is simply achieved by multiplying the currents in the original configuration ($g^* = 0.65$) by a constant value.

TABLE III. Different magnetic induction gradients applied and regimes of effective gravity $\tilde{g}$ explored. The columns present the five different variants of the magnetic field in the Cases g^*. The rows show the non-dimensional gravities g^* defined as the ratio between the effective gravity $\tilde{g}$ and the usual gravity acceleration $g = 9.8$ m/s^2, and the values of $\nabla_z B$ evaluated at $r = 0$ (i.e., the coils' axis) denoted G_z.

$g^* = \tilde{g}/g$	G_z (G/m)	B_0 (G)
0.43 ± 0.02	-476 ± 42	37 ± 1
0.65 ± 0.02	-286 ± 25	22 ± 1
0.77 ± 0.02	-191 ± 16	15 ± 1
0.80 ± 0.02	-171 ± 15	13 ± 1
0.90 ± 0.02	-95 ± 8	7 ± 1

The exploration of settling regimes is performed by independently changing the effective gravity and the fluid viscosity according to the following protocol. For a given value of fluid viscosity, all the previous values of $\tilde{g}$ are applied to vary Galileo number. In this way, with a fixed viscosity, the Galileo number can be modified by varying the effective gravity between 65% and 100% of its value at $g = 9.8$ m/s^2. The range of Ga values explored is $[100, 280]$.

In the remainder of this article, non-dimensional parameters are denoted by a superscript asterisk. Spatial variables are normalized by particle diameter $x^* = x/d_p$, velocities are normalized by the buoyancy velocity $v^* = v/U_g = v/\sqrt{|\Gamma - 1|\tilde{g}d_p}$, and time is normalized by the response time of the particles $\tau_g = d_p/U_g$.

Finally, the trajectory angle is defined as the ensemble average of the angle between a linear fit to each trajectory and the vertical. The trajectory planarity is quantified by the ratio of eigenvalues λ_2/λ_1 (with $\lambda_1 \geq \lambda_2$) of the non-dimensional perpendicular (to gravity) velocity correlation matrix, defined as[38]:

$$\langle \mathbf{v}^*_\perp \ \mathbf{v}^{*\mathrm{T}}_\perp \rangle = \begin{bmatrix} < {v^*_x}^2 > & < v^*_x v^*_y > \\ < v^*_y v^*_x > & < {v^*_y}^2 > \end{bmatrix}, \tag{8}$$

with $v^* = v/U_g$. Perfect planar (non-planar) trajectories yield λ_2/λ_1=1 (=0), while the fractions represent intermediate cases.

B. Terminal Velocity & Effective Gravity Homogeneity

It is important to verify that the particles reach a terminal velocity, and that there is no global deviation caused by the magnetic induction gradient inhomogeneities measured in Section II C. In this sense, Fig. 4 presents some examples of settling velocity, represented by particle Reynolds numbers ($Re_p = v_s d_p/\nu$, with v_s the velocity component parallel to gravity), for various amplitudes of the applied magnetic gradient in Cases g^*, which correspond to various values of the effective gravity. Two examples of Case g_0 at two different values of

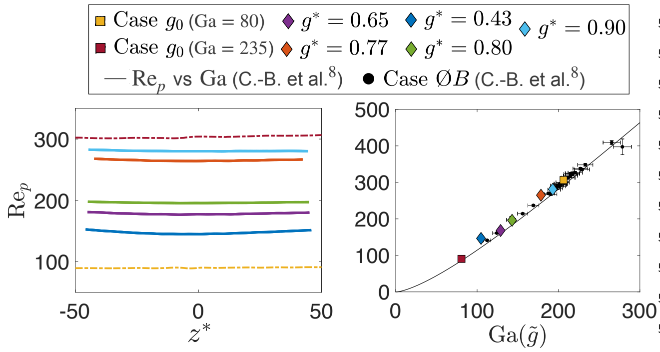

FIG. 4. Particle Reynolds number ($Re_p = v_s d_p/\nu$, with v_s the velocity component parallel to gravity) versus the non-dimensional distance to origin z^* (panel a) and versus the Galileo number computed with the corresponding effective gravity (panel b), for all the variants of external magnetic fields studied. (a) Representative particle Reynolds number from independent realizations for the following cases: g_0 at $\mathrm{Ga}(\tilde{g}) = 235 \pm 7$ (red-violet dashed line) and $\mathrm{Ga}(\tilde{g}) = 80 \pm 5$ (yellow dashed line); $g^* = 0.43$ at $\mathrm{Ga}(\tilde{g}) = 105 \pm 5$ (blue line); $g^* = 0.65$ at $\mathrm{Ga}(\tilde{g}) = 129 \pm 5$ (purple line) ; $g^* = 0.77$ at $\mathrm{Ga}(\tilde{g}) = 178 \pm 5$ (red line); $g^* = 0.80$ at $\mathrm{Ga}(\tilde{g}) = 143 \pm 5$ (green line); and $g^* = 0.90$ at $\mathrm{Ga}(\tilde{g}) = 193 \pm 7$ (cyan line). (b) Particle Reynolds number versus Galileo number, alongside the theoretical settling velocity computed from the correlation presented in Cabrera-Booman et al.[8] and the reference data of Case $\emptyset B$[8].

Ga (80 and 235) are also shown to illustrate the sole effect of rotation blockage in a particle in the Rectilinear (Ga=80) and Planar Rotating (Ga=235) regimes. Note that panel (a) presents single realizations showing the evolution of vertical velocities versus distance to the origin for individual particles at given values of g^* and Ga, while points for the terminal velocity shown in panel (b) are obtained from the ensemble and spatial average of tens of drops.

Fig. 4(a) shows the particle Reynolds number versus the non-dimensional distance to origin z^*, for all the variants of external magnetic fields studied. Note that the different examples shown here were not obtained with the same fluid viscosity, therefore, the corresponding particle Reynolds numbers are not ordered by g^* but by $\mathrm{Ga}(\tilde{g})$. There is a well defined terminal velocity (i.e., the particle Reynolds number is constant) for all magnetic field cases except for Case $g^* = 0.43$ (which corresponds to the case of highest amplitude of applied magnetic field). In that case, Re_p varies as much as 10% along the particle trajectory. This variation is of less than 2% in the other cases, which is in the range of the fluctuations reported in the literature[9] and in the non-magnetic experimental data from Case $\emptyset B$[8]. This indicates that (except for the largest applied field, case $g^* = 0.43$) the applied magnetic field gradient effectively compensates gravity homogeneously, and that the rotation blocking effect does not prevent particles from attaining a well defined terminal velocity. A possible explanation for the lesser quality of Case $g^* = 0.43$ could be related to finite size effects of the coils which were not taken into account in the design of the magnetic field linear profiles and which may enhance the magnetic gradient inhomogeneity.

Fig. 4(b) shows the ensemble and space average of the measured particle Reynolds numbers versus a Galileo number computed using the effective gravity. The marker size represents each data point uncertainty. Black solid circles present the data from the reference case[8] and a solid line presents the Re_p vs Ga correlation law proposed by Cabrera-Booman *et al.*[8], which was inspired from a previous study by Brown *et al.*[39] Note that this correlation has been shown to underestimate the terminal velocity of high density ratio particles[8] by between 5% and 10%, as it can be seen in the figure. We can see that the terminal particle Reynolds numbers of all cases consistently follow the same trend, in good agreement with the proposed correlation. Only the point at $g^* = 0.43$ shows a slight deviation from the global trend, confirming the lesser quality of the magnetically modified gravity in that case.

Overall, it is then concluded that measurements up to $g^* = 0.65$ can be expected to behave analogously to non-magnetic spheres settling at modified gravity (this claim will be confirmed below).

Note regarding the estimation of the effective gravity. The fact that particles reach a terminal velocity allows for the definition of a constant effective gravity, and determining its precise value is crucial. Recall the equation linking $\tilde{g}$ with the experimental parameters (see Section II A):

$$\tilde{g} = g - |\mathbf{M}|\nabla_z|\mathbf{B}|/m. \tag{9}$$

As discussed previously, the value of M can be computed from the manufacturer's data and $\nabla_z B$ was measured. The values of $\tilde{g}$ can then be computed. The method to obtain the effective gravity given by Eq. 9 and detailed above is used throughout the manuscript. However, another way to compute the effective gravity is by the measurement of terminal settling velocity with no external magnetic induction applied $v_{s,0}$ and comparing it to that of particles settling in the same flow but with its gravity modified to $v_{s,M}$. The particle settling velocity can be calculated as:

$$v_s = \sqrt{\frac{mg}{\frac{\pi}{8} C_D(Re_p) d_p^2 \rho_f}}. \tag{10}$$

The ratio $m/(\frac{\pi}{8} d_p^2 \rho_f)$ is identical because the same particles are used, therefore:

$$g^* = \frac{\tilde{g}}{9.8\ m/s^2} = \frac{v_{s,M}^2 C_D(Re_{p,M})}{v_{s,0}^2 C_D(Re_{p,0})}, \tag{11}$$

with $Re_{p,0} = v_{s,0} d_p/\nu$, and $Re_{p,M} = v_{s,M} d_p/\nu$. Then, using usual drag correlations[8,39], it is possible to extract $\tilde{g}$ for all the Cases g^* studied. Values of $\tilde{g}$ that overlap with the computed ones are independently obtained from particle terminal settling velocities.

C. Path instability Results

The different path instabilities of a single spherical magnetic particle settling in a quiescent flow are presented here. The dynamics are controlled by Galileo number (Ga), which varies as the square root of gravity. The goal is to test whether the different settling regimes which have been reported in previous numerical[6,7] and experimental[4,5,8,30] studies (where Ga is classically varied by changing the particle diameter, the particle-to-fluid density ratio, or the viscosity) are consistently recovered when Ga is varied by magnetically modifying the gravity. To further clarify the possible impact of rotation blockage alone, we also consider Case g_0 (homogeneous applied magnetic field) where Ga is classically varied. Measurements in Cases g^* and g_0 are compared to the reference non-magnetic case[8]. First, we qualitatively show the taxonomy of the different type of trajectories observed when spanning Ga in the magnetic case. Then, the trajectory angle and planarity are quantitatively compared to the experimental[8] and numerical[7] data in the non-magnetic reference scenario Case $\emptyset B$.

It is shown that by magnetically changing gravity, the path instability in action can be tuned and that all the classical regimes are recovered in the same range of Ga and with the same trajectory properties than for the reference non-magnetic case.

The state-of-the-art Γ - Ga parameters space taken from Cabrera-Booman *et al.*, alongside the data points explored in the present study are presented in Fig. 5.

It is worth stressing that, as revealed in previous non-magnetic experimental studies (see for instance the recent work by Raaghav *et al.*[30] and Cabrera-Booman *et al.*[8]) the boundaries between regimes in this space of parameters are not always sharp. Some regimes exist in a narrow range of Ga and some regions have been shown to exhibit multi-stability (i.e., several regimes have been reported in similar regions of parameters). This may also be affected by the uncertainty, typically of the order of a few percentage points, with which the Galileo number is determined. This is mostly due to uncertainties of the viscosity in the classical non-magnetic case, with the addition in the present case of the small variability of effective gravity modification due to the 5% variability of the magnetic gradient across the measurement volume previously discussed.

1. Trajectories Geometry

Fig. 6 presents some representative 3D trajectories (first column) alongside a top view (second column). All of these trajectories belong to Case g_0 (rotation blockage and normal gravity), as those of Case g^* present the same dynamics but with shorter trajectories. Each subpanel presents results with Ga in the main four regimes previously identified:

(1) Steady Oblique – Ga = $\{153, 158\}$. Fig. 6(a) presents some trajectories in this regime. Although some trajectories show slight deviations from perfect planarity (the value of the planarity parameter $\sqrt{\lambda_2/\lambda_1}$ will be shown later to be of the order of 0.2 versus 0.05 for Case $\emptyset B$[8]), the trajectories are overall planar and have a well-defined angle with the vertical that, after centering, form a cone in 3D space.

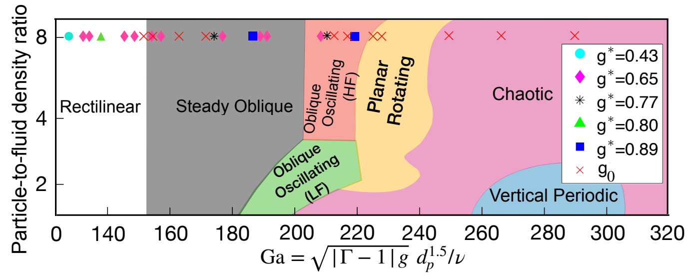

FIG. 5. Particle-to-fluid density ratio (Γ) – Galileo number (Ga) space of parameters. Alongside the data points measured in this study taken from Cabrera-Booman *et al.*[8]

(2) Oblique Oscillating – Ga = 206 (Fig. 6(b)). Trajectories at Ga = 206 would be expected to be in the Oblique Oscillating regime according to numerical simulations[7]. Fig. 6(b) presents some oblique oscillating planar trajectories while others are not perfectly planar and resemble the rotating regime *a priori* expected at slightly higher values of Ga.
The trajectories observed at this Galileo number share properties compatible with both the oblique oscillating and the planar or rotating regimes (Fig. 6(c)). As explained at the beginning of this section, it is likely that, considering the 5% uncertainty in Ga, and the vicinity with the frontier to the Planar or Rotating Regime, these measurements could be attributed to either the oblique oscillating or the planar or rotating regime.

(3) Planar or Rotating – Ga = $\{213, 217\}$. Fig. 6(c) presents some trajectories in this regime. They are composed of weakly non-planar trajectories (black) and some helicoids with diameter $D \approx 10$ and pitch $P \approx 500$ (equivalent to those of Case $\emptyset B$). Note that these values are non-dimensionalized by the particle diameter d_p. A bi-stable region is predicted by numerical simulations and has been observed experimentally with non-magnetic particles[8]. It is also confirmed for the case of magnetic spheres for this range of Ga. Apart from the effects on angle and planarity (discussed in Case $\emptyset B$), this subpanel makes explicit the presence of two regimes at these Ga numbers: Helicoid-like trajectories and oblique non-planar ones.

(4) Chaotic – Ga = 275. Finally, the Chaotic regime correctly matches the characteristics found for Case $\emptyset B$: All trajectories are different, non-planar, and oblique.

The taxonomy and range of Ga for which these different trajectories are observed for Cases g^* (when the particle rotation is blocked and there is an effective gravity) are globally indistinguishable from those found in the reference case $\emptyset B$ of non-magnetic particles and those just

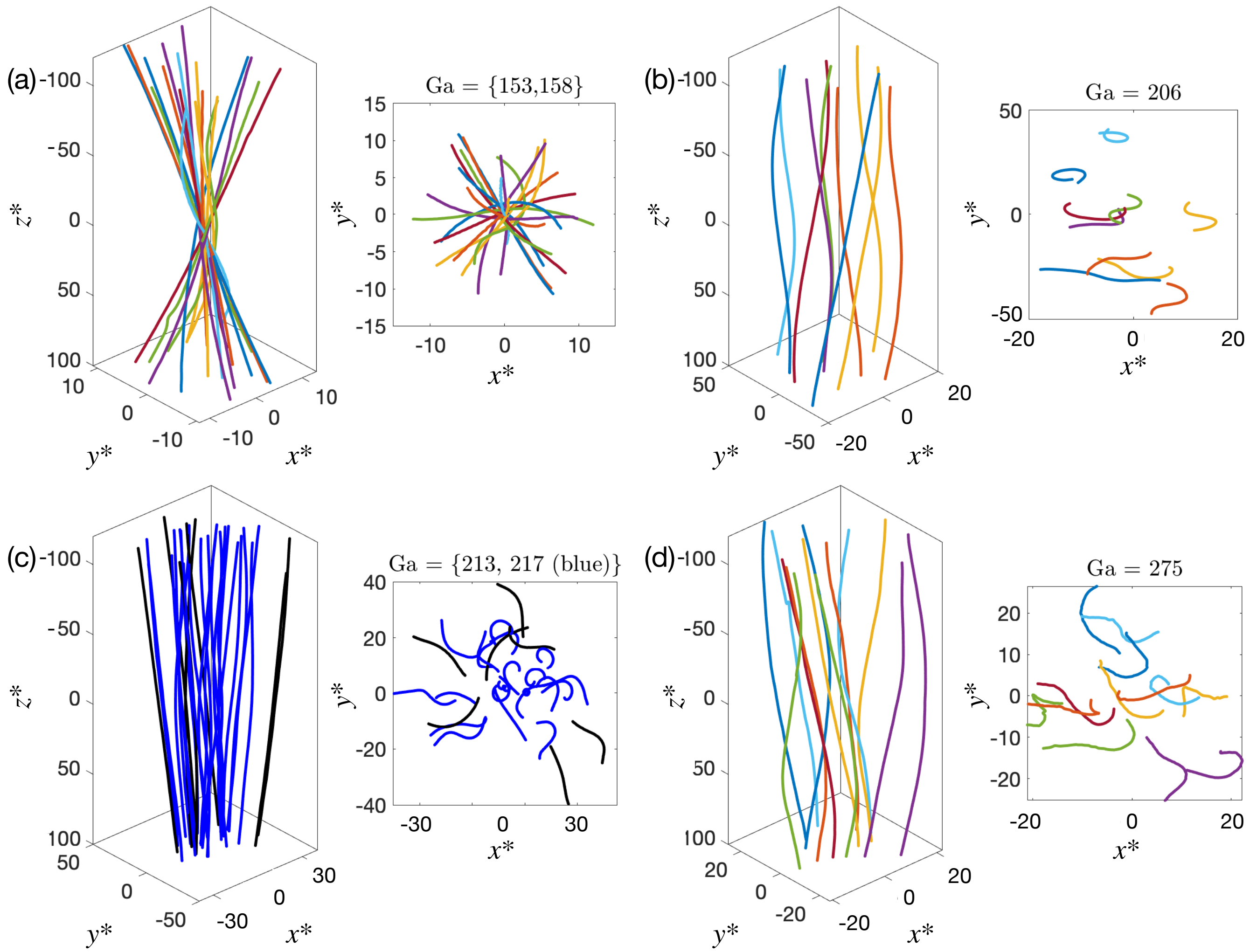

FIG. 6. Representative 3D trajectories, alongside a top view, for results with Ga in the main four regimes presented in the introduction and in Fig.5. Sub-panel (a) – Ga = $\{153, 158\}$, Steady Oblique regime. Sub-panel (b) – Ga = 206, Oblique Oscillating regime. Sub-panel (c) – Ga = $\{213, 217\}$, Planar or Rotating regime. Sub-panel (d) – Ga = 275, Chaotic regime. All these trajectories belong to Case g_0.

described for Case g_0. This supports the hypothesis that rotation blockage and the addition of a magnetic force do not affect the regimes that a settling particle undergoes in a fluid at rest[38]. Furthermore, this supports the idea that the magnetic method to modify the effective gravity presented here indeed modifies gravity without any spurious effect. This is further developed in the coming sections, using quantitative indicators for trajectory planarity and obliqueness in the different regimes.

2. Angle and Planarity of trajectories

Fig. 7 presents the trajectories' angle and planarity versus Ga number, alongside the reference measurements $\emptyset B$ from our group[8] (empty circles). Additionally, the vertical dashed lines show the onsets for the different settling regimes: Rectilinear, Steady Oblique, Oblique Oscillating, Planar or Rotating, and Chaotic. In particular, Fig. 7(b) and Fig. 7(d) present the measurements against a Galileo number Ga($\tilde{g}$) that was calculated with the effective gravity value $\tilde{g}$, whereas Fig. 7(a) and Fig. 7(c) show the measurements as a function of Ga(g) number based on the actual non-perturbed gravity, i.e., $\tilde{g} = 9.8$ m/s^2. Red crosses denote the measurements from Case g_0, for which only the particle rotation is blocked and no net magnetic force modifying the effective gravity exists. The empty circles are the non-magnetic reference data of Case $\emptyset B$[8], and the rest of the markers are the different configurations of Cases g^* and g_0 previously defined, a magnetic field is applied. Note that in the reference case $\emptyset B$ and Case g_0, the points keep the same abscissa between rows because gravity is not modified.

For both the trajectory planarity and angle, it is observed that the data points collapse into a single trend

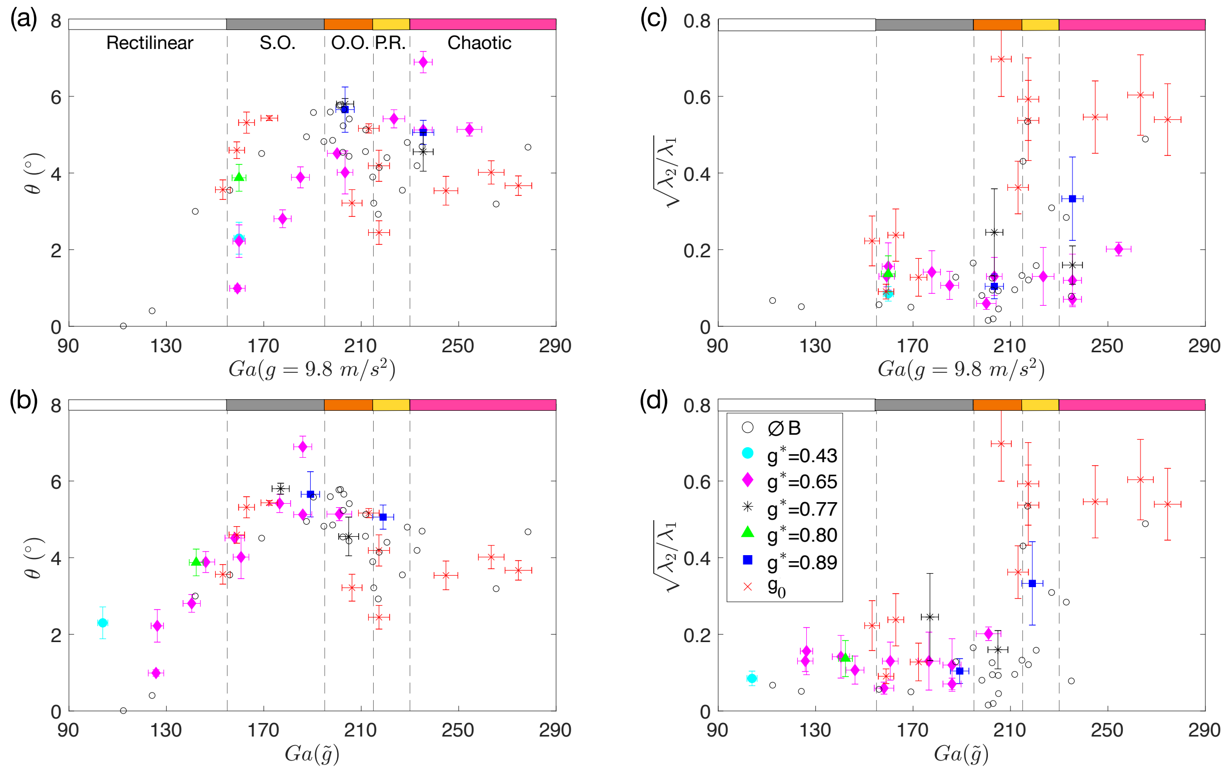

FIG. 7. Trajectory angles with the vertical (a-b) and planarity (c-d) versus Ga number, alongside the reference measurements of Case $\emptyset B$ (empty circles)[8]. Additionally, vertical dashed-lines and color bars[8] show the onsets for the different regimes presented previously following the nomenclature introduced in Cabrera-Booman et al.[8] and Fig. 5. The bottom row shows measurements against a Galileo number that was calculated with the corrected gravity value $\tilde{g}$. The top row presents measurements as a function of a Ga number computed assuming that the gravity did not change with the application of the external magnetic induction (i.e., $\tilde{g} = 9.8$ m/s^2). Finally, different markers and colors are used to distinguish the data points as denoted in the legend.

when the corrected Ga($\tilde{g}$) is used. This is consistent with the reference data case $\emptyset B$, including the transitions between settling regimes, whose detailed description has been reported in Cabrera-Booman et al[8]. It can be seen that Case g_0, for which no magnetic modification to Ga is applied, presents an identical behaviour as the reference Case $\emptyset B$. This implies that there is no measurable effect of the particle rotation blockage on the trajectory angle or planarity. The uniform magnetic gradient strategy allows exploration of Galileo number effects and settling regimes by simply varying the amplitude of the applied field (and thus of its gradient); which is equivalent, in terms of variations of Ga, to viscosity and particle diameter modifications.

Note that the single point with $\tilde{g} = (4.2 \pm 0.2)$ m/s^2 and Ga $= 103$ (light blue circle), which corresponds to the strongest magnetic gradient applied (Case $g^* \approx 0.43$), is off the trend in Fig. 7(b). This is due to the spurious radial magnetic force which, as already pointed out in Section III B, cannot be fully neglected for such strong effective gravity modifications. As a consequence, trajectories in this range of effective gravity acquire a small radial drift and tend to become more oblique.

IV. CONCLUSIONS

This article presents both a magnetic method to modify the gravity on particles in a laboratory and experimental studies on the settling of single spheres in a quiescent flow with modified gravity and blocked spin. A magnetic method to modify gravity is developed, validated, and tested. Its theoretical foundation is presented, including details on how the addition of an external magnetic induction can produce a vertical force that counteracts the gravitational force on a magnetic particle. This experimental method also blocks the perpendicular-to-magnetic field spin of magnetic particles. The homogeneity of the theoretically derived magnetic field needed to compensate gravity is detailed, showing a high level of homogeneity. The coils' positions and currents to produce the desired magnetic field are obtained from a nonlinear fit, and the resulting field measured in the real world is compared to the theoretical field finding good agreement.

The settling of spherical magnets in a quiescent flow is studied and compared to a reference non-magnetic sphere settling measured by our group[8] as both a final validation of the method and a study on the influence of particle spinning on the particle trajectories' dynamics. The latter consists of the analysis of the dynamics of spheres in the parameter space $\Gamma - \mathrm{Ga}$, with a particle-to-fluid density ratio $\Gamma = 8.2$ and Galileo numbers $\mathrm{Ga} \in [100, 280]$. The terminal velocity of particles is discussed for each effective gravity value, showing that particles achieve a homogeneous terminal velocity thus implying that the magnetic method modifies gravity homogeneously. Trajectories in 3D that match benchmark results without gravity are shown for each regime in the path instability parameter space. The results on trajectory angle showed no difference between magnetic and non-magnetic cases, implying that the method to compensate gravity performs well and particle spinning is not relevant for that aspect of the dynamics. On the other hand, trajectory planarity presents minimal differences in the planar or rotating region of the parameter space, although the present measurements are not sufficient to conclude whether there is a rotation blockage effect.

A novel experimental method to compensate gravity on magnetic particles in a fluid has been demonstrated to compensate gravity down to a homogeneous value of 6.37 m/s^2, or 65% of its full value, in the measurement volume without inducing drift or any other spurious effect on the particle dynamics. Note that this value can be further reduced by changing, for instance, the particles. Although not discussed here, this experimental technique can be minimally modified to increase the gravitational pull. There is a considerable value in the method as it allows low-gravity experimentation in a laboratory bench that otherwise would require substantial funding and facilities such as parabolic flights, International Space Station, or drop towers.

This method has great potential for particle-laden turbulent flows where the aim is to disentangle the role of particle inertia and gravity on particle coupling with the surrounding fluid. This requires the modification of the settling properties of the particles independent of the inertial couplings with the fluid. This question is important for unveiling the mechanisms at play during turbulent transport of inertial particles[40], where inertial effects (such as dynamic filtering[41] and preferential concentration[42,43]) are generally parameterized by the particles' Stokes number $St = \tau_p/\tau_\eta$ (with τ_p the particle viscous relaxation time and τ_η the turbulence dissipation time) interplay with particle settling. These effects can, for instance, be parameterized by the settling velocity number $Sv = \tau_p g/u_{\mathrm{rms}}$ (sometimes referred as Rouse number), where g is the acceleration of gravity and u_{rms} is the turbulent fluctuating velocity. Exploring the role of inertia in experiments by varying the Stokes number at fixed turbulent conditions (*i.e.,* for fixed τ_η and u_{rms}) requires variation of the particles' relaxation time τ_p, hence inevitably changing their settling velocity number and the settling properties. Being able to experimentally modify the effective gravity experienced by the particles would give a unique and simple way to truly explore settling velocity number effects at fixed Stokes number.

This method restricts the particle rotation, only allowing for spin in the direction of the magnetic field. On one hand, this is a strong constraint for finite-sized particles where rotational and translational dynamics might be coupled[44,45]. On the other hand, blocking the rotation is also a unique opportunity offered by the magnetic method to disentangle the effects of particle rotation and translation on the global dynamics. Additionally, because the rotational and translational particle dynamics are decoupled in the context of the equation of motion for point particles proposed by Maxey, Riley, and Gatignol[46,47] (MRG), the particle rotation blockage effect generated by this method does not affect its ability to disentangle the role of particle inertia and gravity. The usual rule-of-thumb for finite size effects (i.e., deviations from the MRG framework) suggests that they appear for particles with diameter $d_p > 5\eta$[48] (with the Kolmogorov scale $\eta = (\nu^3/\epsilon)^{1/4}$). Therefore, one can expect the 1 mm particles used here to behave like point particles in flows where $\eta > 200$ μm. Moreover, magnets with sizes of the order of 300 μm are available, therefore allowing for η to be lowered and still be in the MRG framework.

Magnetic anisotropic particles can be considered an infinitesimal dipole with constant magnetic moment M at their center. The fluid torque will be different than in the spherical case described here. For instance, the particle might not align with the magnetic field *instantaneously*. At this time, the smallest spherical permanent magnets have a diameter of 0.5 mm, that in the case of pure water and pure glycerol would result in $Re \approx 90$ and $Re \approx 1 \times 10^{-1}$, respectively. The size of ferromagnetic particles can be as low as 1 μm and their application to this method is detailed in App. C. The use of this method to study collective effects will be complex as inter-particle forces will become dominant when the particles are close. The method will certainly work if the particles are dispersed enough, or encapsulated in large enough non magnetic shells (for instance, wax-encapsulation as done by De La Rosa et al.[27]). However, investigating collective dynamics (such as turbulent preferential concentration) in the presence of additional interparticle interactions is interesting. For instance, droplets in clouds or powders in industrial processes may be charged so that hydrodynamic couplings compete then with interparticle interactions. Although magnetic and electrostatic interactions are different, studying the modification of turbulent clustering in presence of magnetic interactions may still lead to interesting and relevant new discoveries.

Appendix A: Gravity Compensation Theory

1. Equations of Motion

When applying this method to a particle in a fluid the equations of motion need to include hydrodynamical effects. Neglecting added mass and history forces[46,47], the fluid adds drag[39], torque[49], and buoyancy effects yielding the following equations of motion:

$$\mathbf{F} = (m_p - \mathrm{V}\rho_f)g\ \hat{\mathbf{z}} + \mathbf{M}\cdot\nabla\mathbf{B} - \frac{1}{8}C_D\pi d_p^2\rho_f\mathbf{v}|\mathbf{v}|, \quad \text{(E1)}$$

$$\mathbf{T} = -1/64 C_\omega\rho_f\boldsymbol{\omega}|\boldsymbol{\omega}|d_p^5 - \mathbf{M}\times\mathbf{B}, \quad \text{(E2)}$$

with fluid density ρ_f, particle volume V, kinematic viscosity ν, translational (C_D) and rotational (C_ω) drag coefficients, particle velocity $\mathbf{v}$, and angular velocity $\boldsymbol{\omega}$. Finally, note that if the Reynolds number is low (typically below order one[50], i.e., the Stokes regime) the fluid drag and torque are simpler:

$$\mathbf{F} = (m_p - V\rho_f)g\ \hat{\mathbf{z}} - \nabla(\mathbf{M}\cdot\mathbf{B}) - 3\pi d_p\eta\mathbf{v},$$
$$\mathbf{T} = \pi\eta d_p^3\omega - \mathbf{M}\times\mathbf{B}.$$

2. Magnetic Field Derivation

To homogeneously compensate gravity, the magnetic force on gravity's direction ($\mathbf{F}^M\cdot\hat{\mathbf{z}}$) needs to be a constant independent of z, here denoted G_z. Alongside the previous condition, the external magnetic field $\mathbf{B}$ has to be a solution of Maxwell's equations, leading to the following set of equations:

$$\nabla_z\ \mathrm{B} = G_z, \quad \text{(E3)}$$
$$\nabla\cdot\mathbf{B} = 0, \quad \text{(E4)}$$
$$\nabla\times\mathbf{B} = 0. \quad \text{(E5)}$$

The present work focuses on axisymmetric solutions where a linear magnetic induction in $\hat{\mathbf{z}}$ can be proposed, resulting in: $\mathbf{B}(r,z) = B_r(r)\ \hat{\mathbf{r}} + (G_z\ z + B_0)\ \hat{\mathbf{z}}$, in cylindrical coordinates. B_r can be obtained by solving Eq. E4, leading to the following magnetic field induction:

$$\mathbf{B}(r,z) = (-G_z/2\ r)\ \hat{\mathbf{r}} + (G_z\ z + B_0)\ \hat{\mathbf{z}}.$$

This magnetic induction respects the irrotational condition (Eq. E5), whereas Eq. E3 is exactly satisfied only at $r = 0$. The latter is an unavoidable consequence of the solenoidal nature of magnetic fields. A dependence on the distance to the system axis (r) and the position on the axis (z) are then present in the forces acting on the particle:

$$F_z^M(r,z) = M\ \frac{\partial B}{\partial z} = M\ \frac{(G_z z + B_0)G_z}{\sqrt{(G_z)^2/4r^2 + (G_z z + B_0)^2}},$$
$$F_r^M(r,z) = M\ \frac{\partial B}{\partial r} = M\ \frac{r\ (G_z)^2/4}{\sqrt{(G_z)^2/4r^2 + (G_z z + B_0)^2}}. \quad \text{(E6)}$$

Note that $F_r^M(r\to 0) = 0$ and $F_z^M(r\to 0) = MG_z$. Therefore, gravity can be fully compensated at $r = 0$ without any radial force present. Note that this is not in conflict with Earnshaw's theorem[10] because the equilibrium is not stable, i.e., the Laplacian of the magnetic energy is not zero.

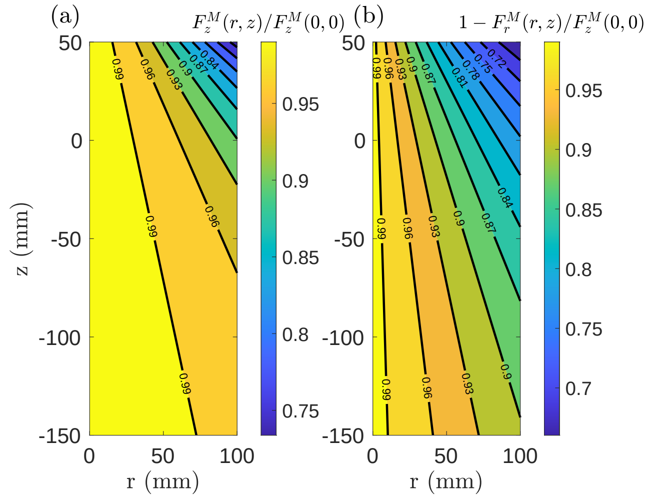

FIG. A.1. Contour plot of the axial (a) and radial (b) component of the theoretical magnetic force, normalized by the axial force at z=0: $F_z^M(r,z)/F_z^M(0,0)$ and 1-$F_r^M(r,z)/F_z^M(0,0)$, respectively.

3. Magnetic Field Homogeneity

Fig. A.1 presents contour plots of $F_z^M(r,z)/F_z^M(0,0)$ and 1-$F_r^M(r,z)/F_z^M(0,0)$. Note that the normalization chosen is $F_z^M(0,0) = MG_z$. Values of $G_z = -250$ G/m, $B_0 = 26$ G, $z \in [-150, 50]$ mm and $M = 4.96\times 10^{-8}$ G^{-1}m^{2}s^{-2} were used to compute the forces from Equations E6, as these are typical magnitudes for the present experimental setup.
The axial component of the force F_z^M has a weak dependence on z and r, as quantified in Fig. A.1(a): A maximum axial force variation of 20% is achieved at $z = 50$ mm and $r = 100$ mm. At $z \in [-150, 0]$ mm and $r \in [0, 20]$ mm, the ranges used in this work, the axial magnetic force has fluctuations below 2%. On the other hand, the radial force F_r^M has a stronger dependence on r and z (see Fig.A.1(b)). When $r = 100$ mm and $z = 50$, the radial force becomes as high as 30% of the reference axial force at the center $F_z^M(0,0)$. At the ranges $z \in [-150, 0]$ mm and $r \in [0, 50]$ mm the maximum value of radial force is reduced to 10% of its axial counterpart.

The relative magnitude of the axial and radial forces can be calculated:

$$\frac{F_r^M(r,z)}{F_z^M(r,z)} = \frac{1}{4}\frac{\mathrm{G_z}\ r}{\mathrm{G_z}\ z + B_0}. \quad \text{(E7)}$$

As the aspiration is to solely counteract gravity, a radial force is not desired and the latter ratio needs to be minimized. There are two ways to achieve it: Keep r small compared to ($z + B_0/\mathrm{G_z}$); and/or have the largest possible value for B_0. The latter approach is ideal because it allows a larger volume (r-z) where the axial force is homogeneous and the radial forces are small. Note that it translates to more current on the coils ($B \propto I$) and, therefore, thicker coil winding that might lead to the necessity of external cooling.

Appendix B: Coils' Input Parameters

The coils' positions (Z_i) and currents (I_i) given by the fit for both cases are presented in Table IV. Note that for Case g_0 only four coils are used as this case does not require more coils to achieve better homogeneity.

For the Cases g^*, the coils are not powered symmetrically because of the need to create a gradient in the magnetic field. To do so, the coils in the region with the highest magnetic field need to have a larger current. It is also important to produce a linear profile of magnetic field around a non-zero values in order to avoid the reorientation of the particle: This would happen because the magnetic field would vanish and reverse direction, forcing the magnetic moment of the particle to re-align.

TABLE IV. Coils' positions and currents given by the fit method for both Cases g_0 and $g^* = 0.65$. The coils' names follow the nomenclature presented in Fig.1.

	Case g_0		Case $g^* = 0.65$	
	Z (cm)	I (A)	Z (cm)	I (A)
Coil 1	✗	✗	26.5	2.28
Coil 2	14.2	4.24	24.5	-1.77
Coil 3	12	0.20	12	1.70
Coil 4	-12	0.16	0	0.52
Coil 5	-14.2	4.46	-24.5	-3.06
Coil 6	✗	✗	-26.5	-1.16

Appendix C: Particle Material Discussion

Equation 1 can be rewritten if one specifies the particle magnetic properties: in the ferromagnetic, paramagnetic, or diamagnetic particle cases $\mathbf{M} \propto \mathbf{B}$, whereas for a permanent magnet (with $B = |\mathbf{B}|$ below its coercive field strength) $M = |\mathbf{M}|$ is constant and $\mathbf{F}^M = \mathbf{M} \cdot \nabla \mathbf{B}$. This work focuses on the latter particle case because magnetic moment values are at least two orders of magnitude larger. This translates into lower external magnetic induction intensities (i.e., less power or smaller coils) to achieve a certain magnetic force.

In particular, the magnetic moment M of a permanent magnet can be computed, if one assumes that the magnetic dipolar moment is dominant, in the following manner:

$$M = \frac{B_{\text{res}} V}{\mu_0}, \tag{E8}$$

where V is the volume of the magnet, μ_0 the vacuum magnetic permeability (note that $\mu_0 \approx \mu_{\text{water}}$) and B_{res} is the remnant magnetic flux density (for the particles used here $B_{\text{res}} = 1.192$ T), in other words the magnet's magnetic flux density when the external coercive field strength is zero.

DECLARATIONS

Funding

This work was in part supported by the U.S. National Science Foundation: Grants NSF-CBET-2224469 and NSF-CBET-2331312 under program managers Drs. Shahab Shojaei-Zadeh and Ronald Joslin, respectively. Additionally, it was supported by the French research program IDEX-LYON of the University of Lyon in the framework of the French program "Programme Investissements d'Avenir": Grant No. hlR-16-IDEX-0005.

Availability of data and materials

Data sets generated during the current study are available from the corresponding author on request.

Ethical Approval

Not applicable.

Conflict of Interest

No conflict of interest.

REFERENCES

[1] Karl Cardin, Christophe Josserand, and Raúl Bayoán Cal. Droplet capture in a fiber array. *Phys. Rev. Fluids*, 8:043601, Apr 2023.

[2] W. Hwang and J.K. Eaton. Turbulence attenuation by small particles in the absence of gravity. *International Journal of Multiphase Flow*, 32(12):1386–1396, 2006.

[3] T Fallon and C B Rogers. Turbulence-induced preferential concentration of solid particles in microgravity conditions. *Experiments in Fluids*, 33(2):233–241, 2002.

[4] M. Horowitz and C. H. K. Williamson. The effect of reynolds number on the dynamics and wakes of freely rising and falling spheres. *Journal of Fluid Mechanics*, 651:251–294, 2010.

[5] C.H.J. Veldhuis and A. Biesheuvel. An experimental study of the regimes of motion of spheres falling or ascending freely in a newtonian fluid. *International journal of multiphase flow*, 33(10):1074–1087, 2007.

[6] G. Bouchet, M. Mebarek, and J. Dušek. Hydrodynamic forces acting on a rigid fixed sphere in early transitional regimes. *European Journal of Mechanics - B/Fluids*, 25(3):321–336, 2006.

[7] W. Zhou and J. Dusek. Chaotic states and order in the chaos of the paths of freely falling and ascending spheres. *International Journal of Multiphase Flow*, 75:205–223, 2015.

[8] F. Cabrera-Booman, N. Plihon, and M. Bourgoin. Path instabilities and drag in the settling of single spheres. *International Journal of Multiphase Flow*, 171:104664, 2024.

[9] O. J. I. Kramer, P. J. de Moel, S. K. R. Raaghav, E. T. Baars, W. H. van Vugt, W.-P. Breugem, J. T. Padding, and J. P. van der Hoek. Can terminal settling velocity and drag of natural particles in water ever be predicted accurately? *Drinking Water Engineering and Science*, 14(1):53–71, 2021.

[10] Earnshaw. *S. Trans. Camb. Phil. Soc.*, page 97–112.

[11] E Beaugnon and R Tournier. Levitation of organic materials. *Nature*, 349(6309):470, 1991.

[12] M. D. Simon and A. K. Geim. Diamagnetic levitation: Flying frogs and floating magnets (invited). *Journal of Applied Physics*, 87(9):6200–6204, 2000.

[13] Magnetic separation techniques in sample preparation for biological analysis: A review. *Journal of Pharmaceutical and Biomedical Analysis*, 101:84–101, 2014. JPBA Reviews 2014.

[14] H. Okada, H. Okuyama, M. Uda, and N. Hirota. Removal of aerosol by magnetic separation. *IEEE Transactions on Applied Superconductivity*, 16(2):1084–1087, 2006.

[15] Separation of mixed waste plastics via magnetic levitation. *Waste Management*, 76:46–54, 2018.

[16] Gradient coil design: A review of methods. *Magnetic Resonance Imaging*, 11(7):903–920, 1993.

[17] S.S. Hidalgo-Tobon. Theory of gradient coil design methods for magnetic resonance imaging. *Concepts in Magnetic Resonance Part A*, 36A(4):223–242.

[18] Jun-Hua Pan, Nian-Mei Zhang, and Ming-Jiu Ni. Instability and transition of a vertical ascension or fall of a free sphere affected by a vertical magnetic field. *Journal of Fluid Mechanics*, 859:33–48, 2019.

[19] Mailfert, Alain, Beysens, Daniel, Chatain, Denis, and Lorin, Clément. Magnetic compensation of gravity in fluids: performance and constraints. *Eur. Phys. J. Appl. Phys.*, 71(1):10902, 2015.

[20] D Chatain, D Beysens, K Madet, V Nikolayev, and A Mailfert. Study of fluid behaviour under gravity compensated by a magnetic field. *Microgravity - Science and Technology*, (3):196–199.

[21] Clément Lorin, Alain Mailfert, Christian Jeandey, and Philippe J. Masson. Perfect magnetic compensation of gravity along a vertical axis. *Journal of Applied Physics*, 113(14):143909, 2013.

[22] V S Nikolayev, D Chatain, D Beysens, and G Pichavant. Magnetic Gravity Compensation. *Microgravity Science and Technology*, 23(2):113–122, 2011.

[23] F Box, E Han, C R Tipton, and T Mullin. On the motion of linked spheres in a Stokes flow. *Experiments in Fluids*, 58(4):29, 2017.

[24] Jérémy Vessaire, Nicolas Plihon, Romain Volk, and Mickaël Bourgoin. Sedimentation of a suspension of paramagnetic particles in an external magnetic field. *Phys. Rev. E*, 102:023101, Aug 2020.

[25] Eric E. Keaveny and Martin R. Maxey. Spiral swimming of an artificial micro-swimmer. *Journal of Fluid Mechanics*, 598:293–319, 2008.

[26] V. Kumaran. Rheology of a suspension of conducting particles in a magnetic field. *Journal of Fluid Mechanics*, 871:139–185, 2019.

[27] H. M. De La Rosa Zambrano, G. Verhille, and P. Le Gal. Fragmentation of magnetic particle aggregates in turbulence. *Phys. Rev.s Fluids*, 3:084605, Aug 2018.

[28] Mathieu Jenny, Gilles Bouchet, and Jan Dusek. Nonvertical ascension or fall of a free sphere in a newtonian fluid. *Physics of Fluids*, 15(1):L9–L12, 2003.

[29] M. Jenny, J. Dusek, and G. Bouchet. Instabilities and transition of a sphere falling or ascending freely in a newtonian fluid. *Journal of Fluid Mechanics*, 508:201–239, 2004.

[30] Shravan K.R. Raaghav, Christian Poelma, and Wim-Paul Breugem. Path instabilities of a freely rising or falling sphere. *International Journal of Multiphase Flow*, 153:104111, 2022.

[31] Values of $G_z = -250$ G/m, $B_0 = 26$ G, $z = 100$ mm, and $M = 4.96 \times 10^{-8}$ G^{-1}m^{2}s^{-2}.

[32] R.P Chhabra, S Agarwal, and K Chaudhary. A note on wall effect on the terminal falling velocity of a sphere in quiescent newtonian media in cylindrical tubes. *Powder Technology*, 129(1):53–58, 2003.

[33] M. Bourgoin and S. G. Huisman. Using ray-traversal for 3d particle matching in the context of particle tracking velocimetry in fluid mechanics. *Rev. Sci. Instr.*, 91(8):085105, 2020.

[34] Nicholas T Ouellette, Haitao Xu, and Eberhard Bodenschatz. A quantitaive study of three-dimensional Lagrangian particle tracking algorithms. *Experiments in Fluids*, 39:722, 2005.

[35] Roger I. Tanner and Shaocong Dai. Particle roughness and rheology in noncolloidal suspensions. *Journal of Rheology*, 60(4):809–818, 2016.

[36] Yu Zhao and Robert H. Davis. Interaction of sedimenting spheres with multiple surface roughness scales. *Journal of Fluid Mechanics*, 492:101–129, 2003.

[37] Indresh Rampall, Jeffrey R. Smart, and David T. Lighton. The influence of surface roughness on the particle-pair distribution function of dilute suspensions of non-colloidal spheres in simple shear flow. *Journal of Fluid Mechanics*, 339:1–24, 1997.

[38] Wei Zhou. *Instabilités de trajectoires de spheres, ellipsoides et bulles*. PhD thesis, 2016.

[39] Phillip P. Brown and Desmond F. Lawler. Sphere drag and settling velocity revisited. *Journal of Environmental Engineering*, 129(3):222–231, 2003.

[40] Luca Brandt and Filippo Coletti. Particle-Laden Turbulence: Progress and Perspectives. *Annual Review of Fluid Mechanics*, 54(1):159–189, 2022.

[41] C. M. Tchen. *Mean value and correlation problems connected with the motion of small particles suspended in a turbulent fluid*. PhD thesis, TU Delft, 1947.

[42] Kyle D. Squires and John K. Eaton. Preferential concentration of particles by turbulence. *Physics of Fluids A: Fluid Dynamics*, 3(5):1169–1178, 1991.

[43] F. Falkinhoff, M. Obligado, M. Bourgoin, and P. D. Mininni. Preferential concentration of free-falling heavy particles in turbulence. *Phys. Rev. Lett.*, 125:064504, Aug 2020.

[44] Robert Zimmermann, Yoann Gasteuil, Mickael Bourgoin, Romain Volk, Alain Pumir, and Jean-François Pinton. Rotational intermittency and turbulence induced lift experienced by large particles in a turbulent flow. *Physical review letters*, 106(15):154501, 2011.

[45] Varghese Mathai, Matthijs WM Neut, Erwin P van der Poel, and Chao Sun. Translational and rotational dynamics of a large buoyant sphere in turbulence. *Experiments in fluids*, 57:1–10, 2016.

[46] Martin R. Maxey and James J. Riley. Equation of motion for a small rigid sphere in a nonuniform flow. *The Physics of Fluids*, 26(4):883–889, 1983.

[47] R. Gatignol. The faxén formulae for a rigid particle in an unsteady non-uniform stokes flow. *J. Méc. Theor. Appl.*, 1(143), 1983.

[48] Haitao Xu and Eberhard Bodenschatz. Motion of inertial particles with size larger than kolmogorov scale in turbulent flows. *Physica D: Nonlinear Phenomena*, 237(14):2095–2100, 2008. Euler Equations: 250 Years On.

[49] Nikolay Lukerchenko, Yury Kvurt, Alexander Kharlamov, Zdenek Chara, and Pavel Vlasak. Experimental evaluation of the drag force and drag torque acting on a rotating spherical particle moving in fluid. *Journal of Hydrology and Hydromechanics*, 56:88–94, 01 2008.

[50] F. Cabrera, M. Z. Sheikh, B. Mehlig, N. Plihon, M. Bourgoin, A. Pumir, and A. Naso. Experimental validation of fluid inertia models for a cylinder settling in a quiescent flow. *Phys. Rev. Fluids*, 7:024301, Feb 2022.